Available online at www.sciencedirect.com
ScienceDirect
Trans. Nonferrous Met. Soc. China 34(2024) 3536−3553
Transactions of Nonferrous Metals Society of China
www.tnmsc.cn

Microstructure evolution and tensile behavior of balanced Al−Mg−Si alloy with various homogenization parameters

Dong JIN[1], Hong-ying LI[1], Zhi-xiang ZHU[2], Chang-long YANG[3], Yao-jun MIAO[4], Chao XU[3], Bao-an CHEN[2], Zhen LIU[5]

1. School of Materials Science and Engineering, Central South University, Changsha 410083, China;
2. State Key Laboratory of Advanced Power Transmission Technology, State Grid Smart Grid Research Institute Co., Ltd., Beijing 102209, China;
3. State Grid Liaoning Electric Power Supply Co., Ltd., Shenyang 110042, China;
4. Jiangsu Zhongtian Technology Co., Ltd., Nantong 226010, China;
5. China Electric Power Research Institute Co., Ltd., Beijing 100192, China

Received 5 April 2023; accepted 13 November 2023

Abstract: The effects of homogenization parameters on the microstructure evolution and tensile behavior of a balanced Al−Mg−Si alloy were investigated using the optical microscope, scanning electron microscope, X-ray diffraction, electron probe microanalyzer, differential scanning calorimetry, electrical conductivity test, and tensile test. The results show that Mg_2Si and β-AlFeSi are the main intermetallic compounds in the as-cast structure, and Mg solute microsegregation is predominant inside the dendrite cell. The prediction of the full dissolution time of Mg_2Si by a kinetic model is consistent with the experiment. The β-AlFeSi in the alloy exhibits high thermal stability and mainly undergoes dissolution and coarsening during homogenization at 560 °C, and only a small portion is converted to α-AlFeSi. The optimal homogenization parameters are determined as 560 °C and 360 min, when considering the evolution of microstructure and resource savings. Both the strength and ductility of the alloy increased after homogenization.
Key words: Al−Mg−Si alloy; homogenization; kinetic model; Fe-bearing phase; tensile behavior

1 Introduction

The age-hardenable Al−Mg−Si conductor alloys, such as AA6101 and AA6201, are widely used for overhead transmission lines in the electrical industry owing to their good combination of high strength and acceptable electrical conductivity (EC) [1−4]. Most Al−Mg−Si alloys are cast using semi-continuous or continuous casting technology, with a cooling rate decreasing from the mold surface into the center within the range of 20−0.5 °C/s [5,6]. Nevertheless, dendrite segregation, low melting point eutectic particles, and insoluble Fe-bearing particles would develop in the as-cast structure during rapid solidification, thereby harming the extrudability and surface quality of rods [7,8]. Therefore, it is necessary to homogenize the casting Al−Mg−Si alloy for the purpose of eliminating dendrite segregation, dissolving the low melting point eutectic particles, and minimizing the detrimental effects of Fe-bearing particles [9−11].

The content of Mg and Si and the Mg/Si ratio affect the formation of low melting point eutectic phases and thus the selection of the homogenization parameters [12,13]. For the Mg-excess or balanced alloy, binary eutectic (α-Al+Mg_2Si) is formed at 595 °C during solidification [12,14]. For the Si-excess

Corresponding author: Hong-ying LI, Tel: +86-731-88879341, E-mail: lhying@csu.edu.cn
DOI: 10.1016/S1003-6326(24)66624-0

alloy, the ternary eutectic (α-Al+Si+Mg_2Si) may be formed at 555 °C [12]. It is clear that a lower homogenization temperature should be selected for the Si-excess alloy. The dissolution of Mg_2Si particles is the main process during homogenization treatment. Therefore, it is essential to study the dissolution kinetics of the Mg_2Si particles [15−17]. ROMETSCH et al [18] modeled the dissolution of Mg_2Si in Al−Si−Mg alloys based on the Fick's first law and predicted that less than 1 h at 540 °C is sufficient to dissolve Mg_2Si fully. SAMARAS et al [19] simulated the dissolution process of Mg_2Si during homogenization in the AA6061 alloy by employing computational kinetics for the solution of the multicomponent diffusion equations and predicted that the full dissolution time of Mg_2Si at 580 °C is 2 h. ZHANG et al [20] modeled the dissolution of second phases (Mg_2Si, Si, and Q) in the Al−Mg−Si−Cu alloy by combining the classical diffusion-controlled dissolution equation with the JMA-like equation and established the relationship between the complete dissolution time and particle size.

Fe is the principal impurity element of the Al−Mg−Si alloys and generally exists as intermetallic compounds (IMCs), mainly α-AlFeSi and β-AlFeSi [21−23]. Previous research suggested that α-AlFeSi has various stoichiometries designated as Al_8Fe_2Si, $Al_{12}Fe_3Si_2$, or $Al_{12.7}Fe_3Si_{1.0}$, with the Fe:Si ratio in the range of ~(1.28−3.83):1 (at.%) [24,25]. The typical stoichiometry of β-AlFeSi is β-Al_5FeSi with a Fe:Si ratio of 1:1 (at.%) [21−23]. The type of Fe-bearing phase that forms depends on the chemical composition and solidification rates [12,26]. Increasing the Mg and Fe concentrations in the alloy promotes the formation of α-AlFeSi [27,28], while increasing the Si concentration promotes the formation of β-AlFeSi [29]. Moreover, α-AlFeSi dominated at a higher cooling rate but β-AlFeSi at a lower cooling rate for the given alloy composition [26]. The needle-like β-AlFeSi harms mechanical properties and tends to induce micro-cracks and surface defects in extruded profiles, while the globular α-AlFeSi is relatively harmless [21,23]. Hence, it is significant to eliminate the detrimental effect of β-AlFeSi. Numerous studies demonstrated that the transformation of β-AlFeSi to α-AlFe(Mn)Si (β to α) occurs during homogenization for the Mn-added 6xxx series alloys [7,8,21−23]. However, for the Mn-free Al−Mg−Si alloys, it is debatable whether the transformation of β-AlFeSi to α-AlFeSi can happen below 600 °C [10,30]. ZAJAC et al [31] found that the transformation of β to α is suppressed in the low Fe:Si ratio 6xxx alloys. For the Al−Mg−Si conductor alloy, the complete transformation of β to α requires a long soaking time at high temperatures due to its low Fe:Si ratio. However, it is likely to cause overburning of the alloy and increase energy consumption. Therefore, it is very important to study the transformation behavior of β to α for determining the homogenization regime.

Most published works reported the homogenization process of Si-excess Al−Mg−Si−Mn alloys, but there are few studies about the homogenization process of balanced Al−Mg−Si alloys. The present work provides quantitative characterization of the homogenization treatment in a balanced alloy with little Fe impurity, focusing on the evolution of the (Mg, Si)-bearing phases and Fe-bearing phases in this relatively pure alloy system during homogenization. In addition, the tensile test is used to illustrate the effect of homogenization treatment on the improvement of the ductility of the alloy and to reveal the reasons by analyzing the fracture behavior. This study aims to inform the industrial processing of high-performance Al−Mg−Si conductor materials.

2 Experimental

The material used in this study was prepared by the commercially pure Al (99.7 wt.%), pure Mg (99.9 wt.%), and Al−20wt.%Si master alloy. Pure Al was completely melted in a graphite crucible with a resistance furnace at 750 °C, and then Al−20wt.%Si master alloy and pure Mg were added to liquid Al in sequence. When the melted alloy was slowly cooled to 720 °C, it was degassed and refined using C_2Cl_6. After being stabilized for 10 min at 720 °C, the melted alloy was poured into a water-cooling mold to obtain ingots with dimensions of 40 mm × 160 mm × 250 mm. A relatively high cooling rate of ~20 °C/s was obtained by adopting the water-cooling mold, which is close to the upper limit cooling rate of DC casting. The composition of the ingot obtained by an inductively coupled plasma optical emission spectrometer (ICP-OES) is given in Table 1. The Mg/Si mass ratio of the alloy

is close to 1.73, which is a balanced Al−Mg−Si alloy.

Table 1 Chemical composition of studied alloy (wt.%)

Mg	Si	Fe	B	Cr
0.95	0.55	0.10	0.031	0.0008
Mn	V	Ti	Other	Al
0.0020	0.0023	0.0023	≤0.01	Bal.

Two sets of single-stage homogenization experiments were conducted on the studied alloy to study the effects of the homogenization parameters on the microstructure. One focused on the effect of homogenization temperature on the second phase. The range of homogenization temperature can be estimated according to the Al−Mg_2Si pseudo-binary phase diagram as 550−595 °C [14]. The lower limit of this temperature range corresponds to the solvus and the upper limit corresponds to the solidus. 550, 560, 570, 580, and 590 °C were selected as the experimental temperatures. The as-cast samples were heated to the given temperatures at a rate of 5 °C/min and then homogenized at each temperature for 200 and 480 min. The other was carried out by varying the homogenization time from 0 to 960 min at 560 °C. The EC values were measured for samples homogenized at 560, 570, and 590 °C, respectively, to monitor the evolution of the microstructure. In the heating-up stage, the samples were heated to the assigned temperature (130, 230, 330, 430, and 530 °C) and then quenched in water, followed by EC testing. In the isothermal holding stage, the EC values of samples were also measured after water quenching.

All samples were taken from the equiaxed zone of ingots. The grain structure of the alloy was characterized by a Leica DMI 300M polarized optical microscope (OM) after anodizing using Barker's reagent. The microsegregation of the alloy was revealed using Weck's reagent [15,32]. The microsegregation of alloy elements was semi-quantitatively analyzed by a JEOL JXA−8230 electron probe microanalyzer (EPMA). The microstructure and fracture morphologies were examined by a Tescan MIRA3 scanning electron microscope (SEM) with an energy dispersive X-ray spectroscopy (EDS) detector. The types of secondary phases were identified by X-ray diffraction (XRD) tests using a Rigaku D/max 2550 diffractometer with Cu K_α radiation. The types of Fe-bearing phases were classified by the stoichiometric differences in the Fe: Si atomic ratios as determined by EDS.

Differential scanning calorimetry (DSC) was used to analyze the dissolution temperature of the second phase to determine the homogenization temperature. The DSC test was carried out using a NETZSCH STA 449C thermal analysis system with a scanned temperature interval from room temperature to 700 °C under the protection of an argon atmosphere. The heating rate is 10 °C/min. The EC of samples was measured using an eddy current conductivity meter with a frequency of 60 kHz at 20 °C. Tensile tests were performed using an UTM5105 universal testing machine at room temperature with a strain rate of 5×10^{-3} s^{-1}. The tensile samples, 3.4 mm in width and 3 mm in thickness, were machined from the as-cast and homogenized billets. All tensile tests were performed on at least three samples for the same condition. The volume fraction and dimension parameters of IMCs were measured using Image-Pro Plus 6.0 software. Five randomly selected SEM images were measured for each sample.

3 Results

3.1 Microstructure of as-cast alloy

Figure 1 shows the microstructure of the as-cast alloy. The OM image of the as-cast alloy exhibits equiaxed dendritic morphology (Fig. 1(a)). The average grain size and secondary dendrite arm spacing (SDAS) are (295.2±66.6) μm and (58.4±10.5) μm, respectively. After etching with Weck's reagent, the microsegregation inside the dendrite cell is revealed by a color difference (Fig. 1(b)). Three types of IMCs with different morphologies and contrasts are formed at the α(Al) matrix (Fig. 1(c)). The chemical compositions of the IMCs marked in Fig. 1(c) are listed in Table 2. The XRD and EDS results suggest that the dark phase with a skeleton-like shape is Mg_2Si and the bright phase with a needle-like shape is β-AlFeSi. The atomic ratio of Fe: Si in the EDS results of β-AlFeSi (0.79) is slightly lower than its stoichiometric ratio because of the interference from the surrounding Mg_2Si particles. In addition, the dark Mg-bearing phase without Si is also found in the dendrite cell (Fig. 1(c)).

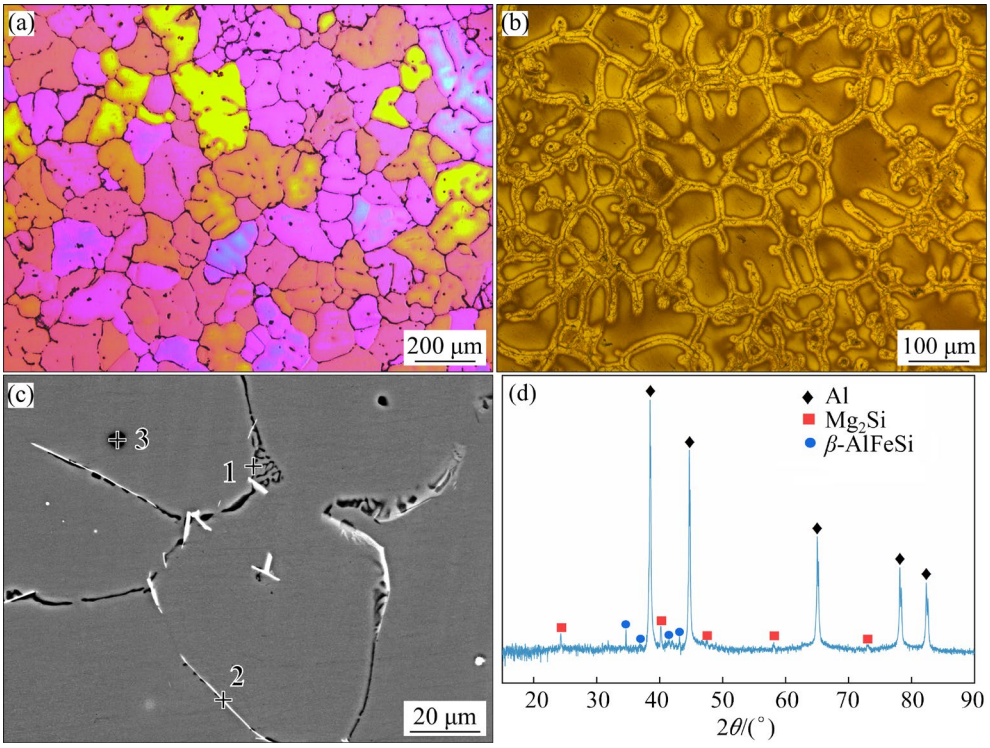

Fig. 1 Initial microstructure of as-cast alloy: (a) Polarized OM image; (b) OM image after etching with Weck's reagent; (c) SEM image; (d) XRD pattern

Table 2 Chemical composition of IMCs measured by EDS shown in Fig. 1(c)

Point No.	Content/at.%				Phase type
	Al	Mg	Fe	Si	
1	63.83	20.91	0	15.26	Mg_2Si
2	82.80	0.75	7.28	9.17	β-AlFeSi
3	69.07	30.93	0	0	Mg-bearing phase

The solute microsegregation in dendrite cells is semi-quantitatively analyzed by EPMA linear scanning, as shown in Fig. 2. It is obvious that the Mg, Si, and Fe elements mainly segregate at dendrite cell boundaries and form IMCs, mainly Mg_2Si and β-AlFeSi (Fig. 2(a)). To reveal the solute microsegregation within the dendrite cell, EPMA linear scanning was performed. As shown in Fig. 2(b′), the horizontal dashed lines indicate the mean measured solute concentrations for Mg, Si, and Fe, respectively. The results indicate that the Mg concentration increases gradually from the center of the dendrite cell to its edge and is lower than the bulk alloy composition of 1.04 at.%. The Si microsegregation is merely detected near the dendrite cell boundary and is lower than the bulk composition of 0.52 at.%. Besides, the Si concentration within the dendrite cell is close to zero. Apparently, there is no Si concentration gradient within the dendrite cell similar to that of Mg. Furthermore, the concentration of Fe remains constant within the dendrite cell and close to zero because of its low solid solubility in the Al matrix (~0.02 at.%) [33].

The DSC analysis is conducted on the as-cast samples in order to determine the upper limit of homogenization temperature, as shown in Fig. 3. It can be seen that there are two obvious endothermic peaks. The first peak with a small thermal effect is caused by the dissolution of eutectic Mg_2Si and its initial temperature (T_i) corresponding to the onset of the melting of Mg_2Si is 578.6 °C. Therefore, the maximum homogenization temperature should be lower than this temperature in order to avoid overburning. The second peak with a large thermal effect corresponds to the melting of the Al matrix.

3.2 Microstructural evolution during homogenization

Figure 4 shows the EC increment curves of the studied alloy during homogenization at 560, 570, and 590 °C. The EC increment is defined as the

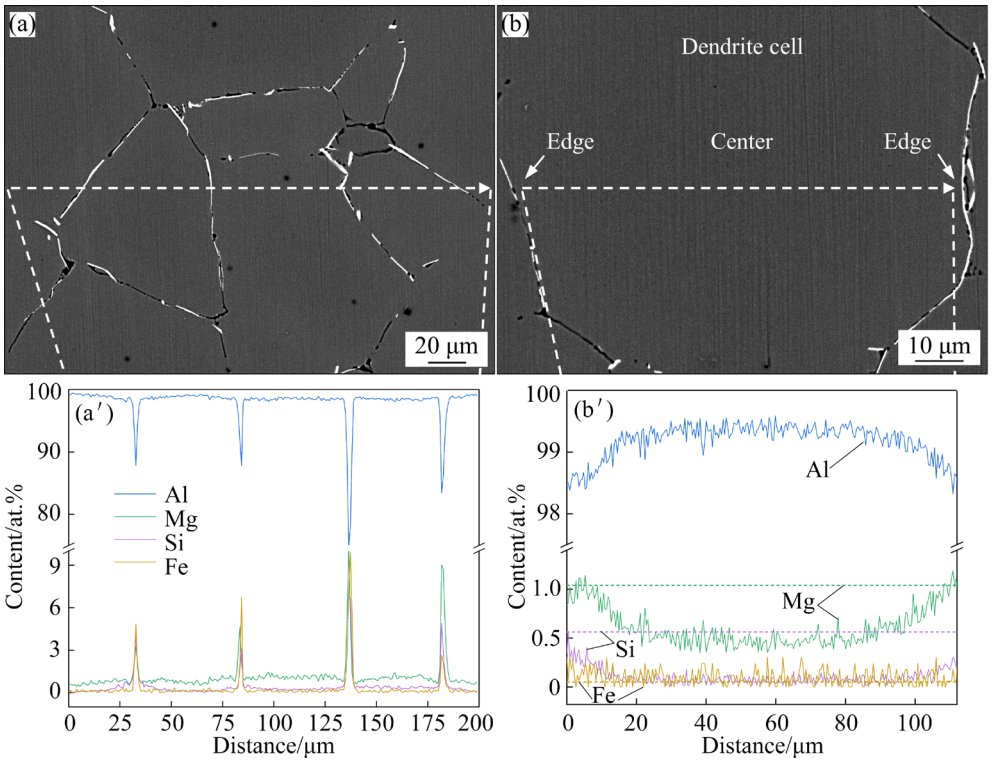

Fig. 2 Composition profiles across multiple dendrite cells (a, a′) and within dendrite region (b, b′) in as-cast alloy, and corresponding mean measured solute concentrations (b′) of bulk alloy composition

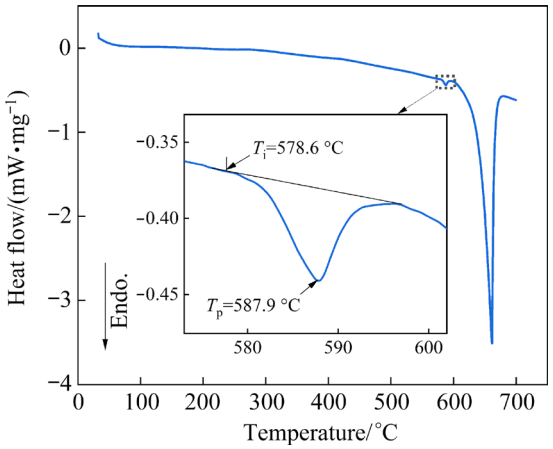

Fig. 3 DSC curve of as-cast alloy (T_p is the peak temperature)

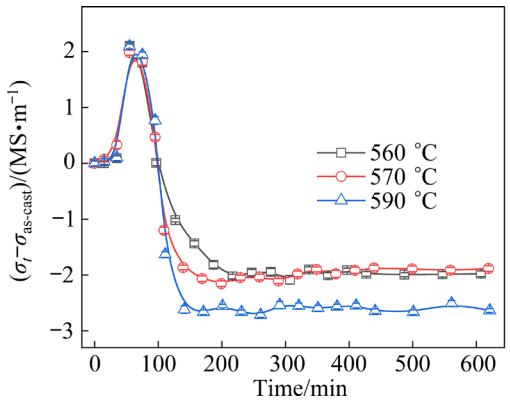

Fig. 4 Electrical conductivity increment curves of Al−Mg−Si alloy during homogenization at 560, 570 and 590 °C (σ_t is the EC of homogenization at time t; $\sigma_{as\text{-}cast}$ is the EC of as-cast sample)

difference between homogenized EC and as-cast EC. At the heating-up stage, the EC increment increases with temperature and peaks at around 330 °C. However, the EC increment decreases rapidly with a further increase in the temperature. At the isothermal holding stage, the EC increment decreases rapidly and finally reaches a stable value. It can be observed that the higher the homogenization temperature, the shorter the time to stability. After homogenization at 560, 570, and 590 °C, the time for EC increment stabilization is about 240, 200, and 140 min, respectively. The stable EC increment value of the sample homogenized at 590 °C is significantly lower than the other two samples. It is deduced that over-burning may have occurred, which is consistent with the result of the DSC analysis (Fig. 3). In 6xxx Al alloys, almost all the Fe will combine with the excess Si and the abundant Al to form Fe-bearing

phases because of its low solubility in the Al matrix [33]. Therefore, it is reasonable to ignore the effect of Fe on EC. The EC mainly reveals the changes in Mg and Si solubility in alloys during homogenization. The precipitation of (Mg, Si)-bearing phases may cause an increase in EC increment during the initial heating-up stage. In the subsequent heating and isothermal holding stages, the dissolution of precipitated (Mg, Si)-bearing phases and eutectic Mg_2Si leads to a decrease in EC increment.

Figure 5 shows the OM images of the alloy after isochronous homogenization at different temperatures for 200 min. After homogenization at 550 and 560 °C, dendritic structure is diminished significantly with thinner and smoother grain boundaries, but some IMCs remain at grain boundaries (Figs. 5(a, b)). When the temperature is 570 °C, the dendritic structure disappears, and the number of IMCs decreases significantly (Fig. 5(c)). The grain structure has no apparent change with the further increase in temperature (data not shown). As shown in Figs. 5(d−f), it can be seen that the color difference within the grains has disappeared, indicating that the solute microsegregation within the grain has been eliminated at test temperatures.

To further determine the evolution of IMCs after isothermal homogenization, the SEM images of the alloy after isochronous homogenization at 550 to 590 °C for 200 min are exhibited in Figs. 6(a−e). It can be seen that the morphology of soluble Mg_2Si changes from a skeleton-like shape to a spherical or rod-like shape to reduce the interfacial area due to the Gibbs−Thomson effect [34]. As the temperature increases, the residual amount of Mg_2Si decreases for a fixed homogenization time. Moreover, overburning caused by the remelting of Mg_2Si is observed when it is homogenized at 590 °C (Fig. 6(e)). The volume fraction of the Mg_2Si phase after isochronous homogenization at 550 to 590 °C for 200 min and 480 min was measured based on the area statistics of the residual phase, as shown in Fig. 6(f). Obviously, increasing the temperature or extending the time will promote the dissolution of the Mg_2Si particles. However, a homogenization temperature close to the melting point of the eutectic Mg_2Si phase would increase the risk of overburning. The dominant types of Fe-bearing particles in homogenized alloys with different temperatures are identified by EDS as β-AlFeSi, as shown in Table 3. The morphology of insoluble β-AlFeSi remains

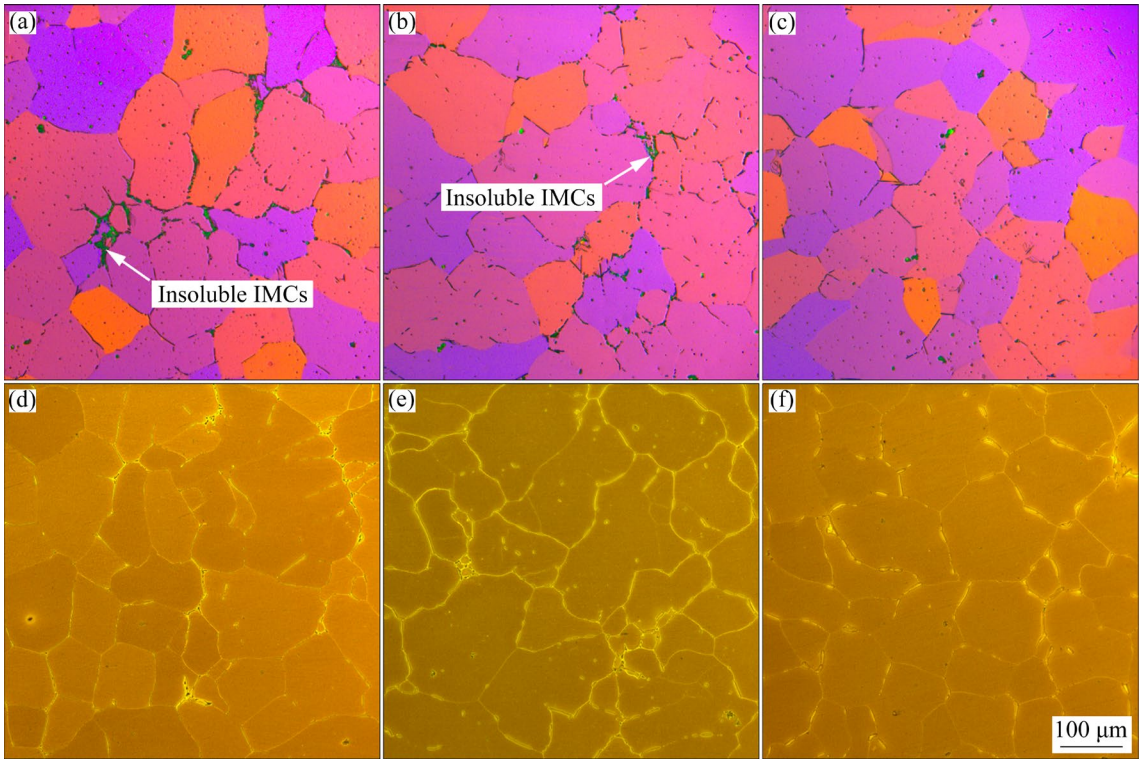

Fig. 5 Polarized OM images of alloy after homogenization at 550, 560 and 570 °C for 200 min (a–c), respectively, and corresponding OM images after etching with Weck's reagent (d−f), respectively

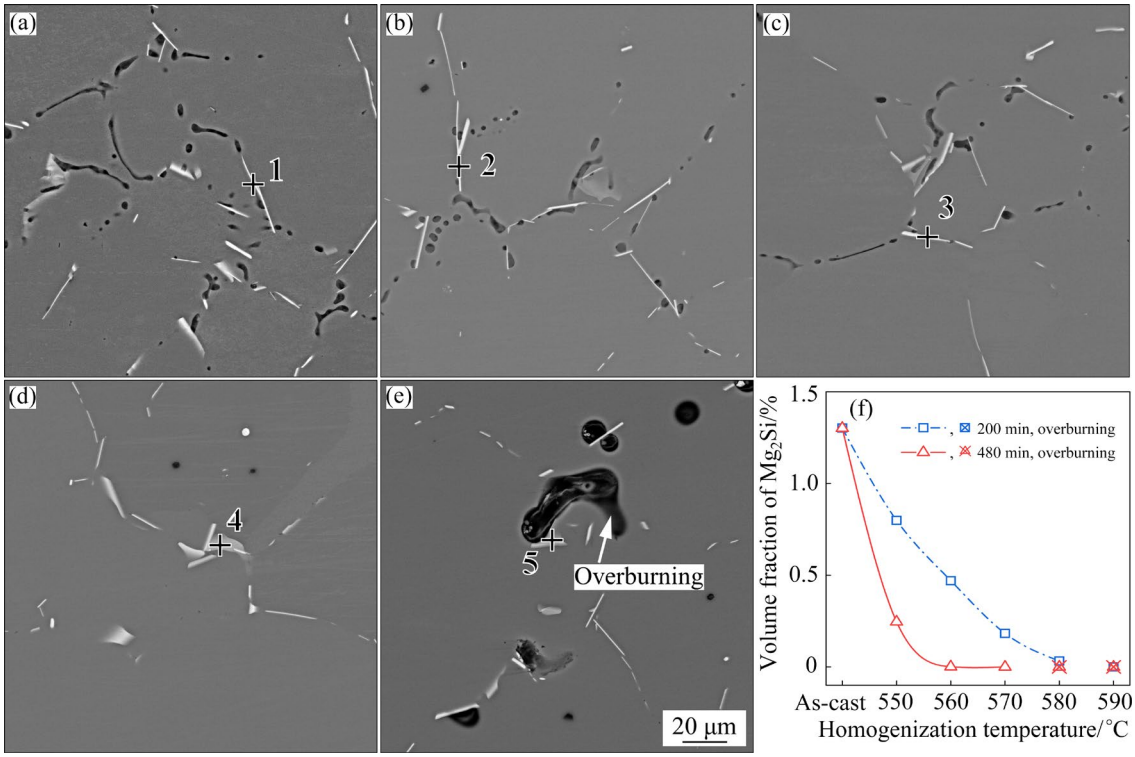

Fig. 6 (a−e) SEM images of alloy after homogenization at different temperatures for 200 min: (a) 550 °C; (b) 560 °C; (c) 570 °C; (d) 580 °C; (e) 590 °C; (f) Volume fraction of Mg_2Si phase after isochronous homogenization at 550 to 590 °C for 200 and 480 min

Table 3 Chemical composition of Fe-bearing particles measured by EDS shown in Fig. 6

Point No.	Homogenization temperature/°C	Content/at.%				Close phase	Fe: Si atomic ratio
		Al	Mg	Fe	Si		
1	550	83.30	0.70	7.20	8.80	*β*-AlFeSi	0.82
2	560	80.86	0.61	8.63	9.90	*β*-AlFeSi	0.87
3	570	81.04	0.65	8.57	9.74	*β*-AlFeSi	0.88
4	580	83.81	0.68	7.52	7.99	*β*-AlFeSi	0.94
5	590	78.08	0.46	10.43	11.03	*β*-AlFeSi	0.95

almost unchanged and needle-like when the homogenization temperature does not exceed 570 °C (Figs. 6(a−c)). When the homogenization temperature reached 580 °C, the *β*-AlFeSi still remained in the matrix and coarsened obviously (Figs. 6(d, e)).

Figure 7 shows the OM images of the alloy after isothermal homogenization at 560 °C for various time. Figures 7(a, b) show the evolution of microstructure during heating. At the end of heating, the IMCs and the dendritic structure almost remain unchanged compared to the as-cast structure (Fig. 7(b)). As shown in Figs. 7(c, d), the soluble IMCs gradually dissolve into the Al matrix with an extension of time. Moreover, some dendrites gradually develop into cell grains with a polygonal shape, which is attributed to the weakened pinning effect of IMCs at grain boundaries due to their morphological changes and dissolution [35]. The grain structure has no significant change when the time further extends to 960 min (data not shown). Figures 7(e, f) show that the solute micro-segregation still exists inside the grains at the end of the heating stage. After homogenization for 150 min, the solute microsegregation within the grain has been eliminated (Fig. 7(g)). The solute distribution within the grains remains constant with extending time (Fig. 7(h)).

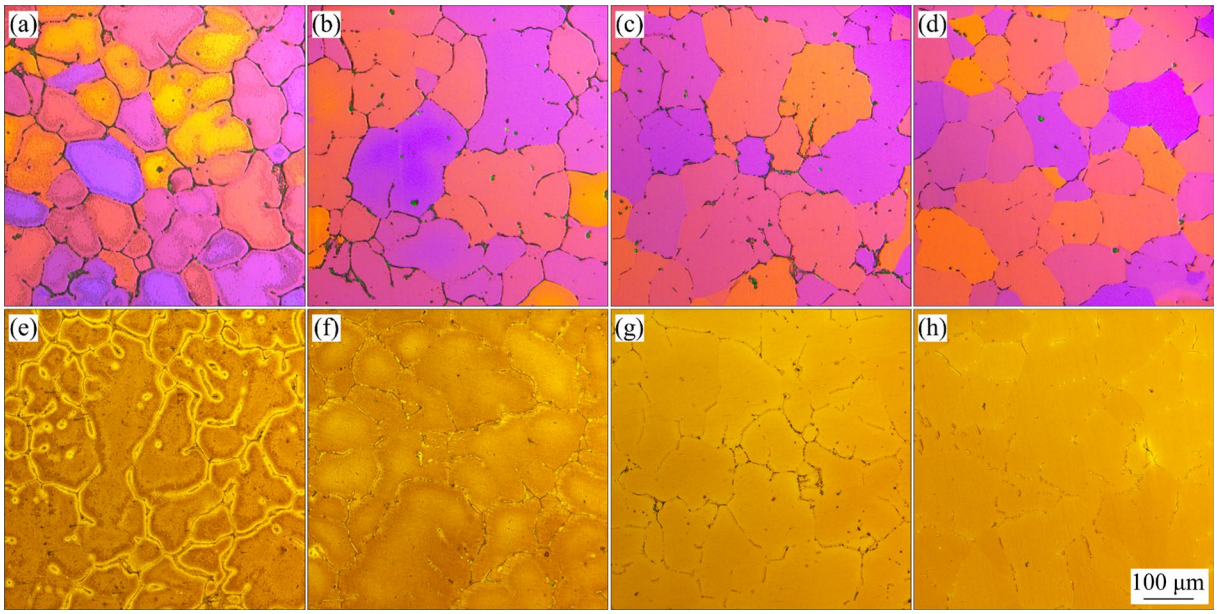

Fig. 7 Polarized OM images of alloy after homogenization at 560 °C for 60 min (time of EC increment peak in Fig. 4), 106 min (time of end of heating), 150 min, and 360 min (a−d), respectively; and corresponding OM images after etching with Weck's reagent (e−h), respectively

Figures 8(a−h) exhibit the evolution of IMCs after homogenization at 560 °C for different time. Figure 8(a) shows the microstructure corresponding to the peak in the EC increment (Fig. 4). The morphology of Mg_2Si remains constant compared to the as-cast alloy. However, the precipitates are formed in the dendrite region, resulting in an increase in EC increment. It also suggests that the matrix of the as-cast alloy is supersaturated. Besides, the particle-free zone (denoted as PFZ) is formed around the dendrite cell boundary and its center. Figures 8(b) and (c) exhibit the enlarged image of the precipitates and the corresponding EDS mappings, indicating that the short rod-like precipitates are likely Si-bearing phases. Figure 8(d) indicates that the short rod-like Si-bearing phase disappears at the end of the heating-up stage and the eutectic Mg_2Si begins to dissolve and spherize. During the isothermal holding stage, the Mg_2Si phase is continuously dissolved with increasing time (Figs. 8(d–h)). After homogenization for 280 min, only sporadic Mg_2Si particles remain at grain boundaries (Fig. 8(f)), and the volume fraction of Mg_2Si is less than 0.07%, which is close to complete dissolution. Even after 960 min of homogenization, there is no overburning in the studied alloy (Fig. 8(h)). Figure 8(i) suggests that the dissolution of Mg_2Si mainly occurs in the first 280 min of homogenization. This result is slightly higher than that of EC increment analysis, and the difference may be caused by the structure homogeneity of the as-cast alloy itself. Figures 8(a−h) also exhibit the morphology evolution of the Fe-bearing phase. It can be seen that the Fe-bearing phases gradually dissolve and coarsen with increasing homogenization time in general. The types of the Fe-bearing phases are further identified by EDS (Table 4). The results show that the dominant Fe-bearing phase in the alloy during the first 360 min of homogenization is β-AlFeSi. A few rounded α-AlFeSi particles are detected in the alloy homogenized for 960 min (Fig. 8(h)). Figure 8(h) also shows that the morphology of some β-AlFeSi particles (e.g., Point 6) is close to that of the α-AlFeSi particles, so it is not reliable to distinguish the two phases by the morphology.

Figure 9 shows the distribution of length, thickness, and aspect ratio of the Fe-bearing phase during homogenization. The Fe-bearing phase contains the β-AlFeSi formed during solidification and the α-AlFeSi formed after the transformation of β to α. The length of the Fe-bearing phase and its range tend to decrease within the first 360 min of homogenization and then remain stable. The thickness of the Fe-bearing phase and its range tend to increase with the extension of homogenization time.

Table 4 Chemical composition of Fe-bearing particles measured by EDS shown in Fig. 8

Pont No.	Homogenization time/min	Content/at.%				Close phase	Fe: Si atomic ratio
		Al	Mg	Fe	Si		
1	60	83.69	1.03	5.95	9.33	β-AlFeSi	0.64
2	106	82.81	0.51	7.27	9.41	β-AlFeSi	0.77
3	150	78.88	0.50	9.09	11.53	β-AlFeSi	0.79
4	280	81.31	0.76	7.47	10.46	β-AlFeSi	0.71
5	360	79.87	0.51	9.69	9.93	β-AlFeSi	0.98
6	960	81.46	0.80	8.46	9.28	β-AlFeSi	0.91
7	960	70.86	0.49	16.67	11.98	α-AlFeSi	1.39

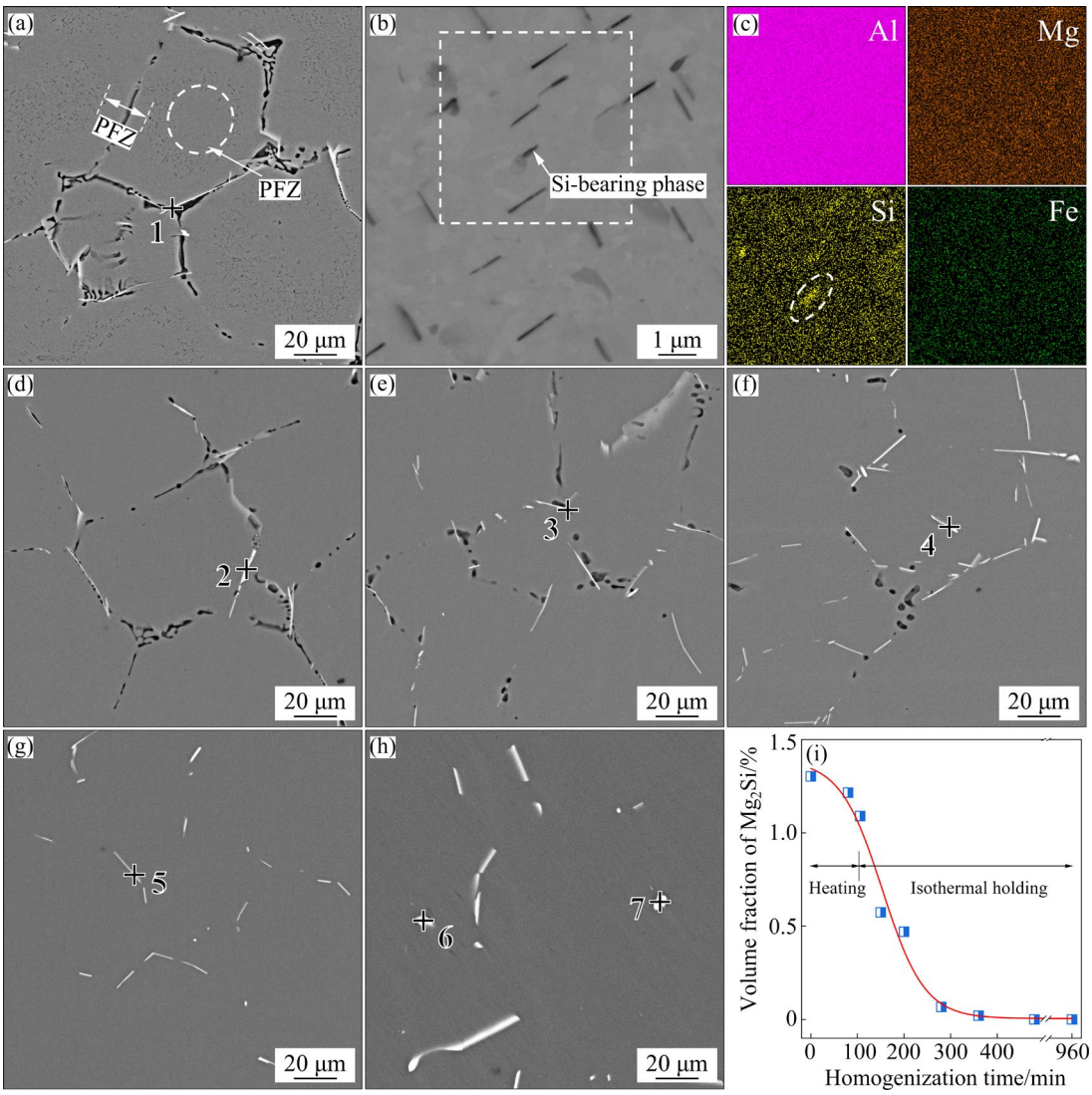

Fig. 8 (a–h) SEM images of alloy after homogenization at 560 °C for various time: (a) 60 min; (b) Rod-like precipitates formed in (a); (c) Corresponding EDS mappings; (d) 106 min; (e) 150 min; (f) 280 min; (g) 360 min; (h) 960 min; (i) Volume fraction of Mg_2Si phase before and after homogenization at 560 °C for different time

The aspect ratio of the Fe-bearing phase and its range continuously decrease with an increase in homogenization time. The above results imply that the dissolution of the Fe-bearing phases occurs during the first 360 min of homogenization, during which the morphology of the Fe-bearing phases

breaks from the long needle-like to the short rod-like (Figs. 8(a−g)). After homogenization for more than 360 min, the Fe-bearing phases get coarsened (Fig. 8(h)).

Figure 10 shows the results of EMPA line scanning after homogenization at 560 °C for 280 min. Compared to the as-cast microstructure (Fig. 2), the Mg_2Si particles dissolve into the matrix, and just some Fe-bearing particles remain at the grain boundaries (Fig. 10(a)). In addition, the concentration gradients of Mg and Si within the grain are eliminated, and the concentrations of Mg and Si in the matrix increase. The measured mean Mg concentration in Fig. 10(b′) agrees well with the bulk alloy composition, indicating that the segregation of Mg is entirely eliminated. However, the measured mean Si concentration is lower than the alloy composition because the Fe-bearing phases cannot be dissolved. The concentration of Fe within the grain of the homogenized alloy remains unchanged compared to the as-cast microstructure.

3.3 Mechanical properties and fracture of as-cast and homogenized alloys

The effects of different homogenization time on the mechanical properties of the studied alloy are evaluated by tensile tests. Figure 11(a) shows the engineering stress−strain curves, and the results are listed in Table 5. The yield strength (YS), ultimate tensile stress (UTS), and elongation (El) of

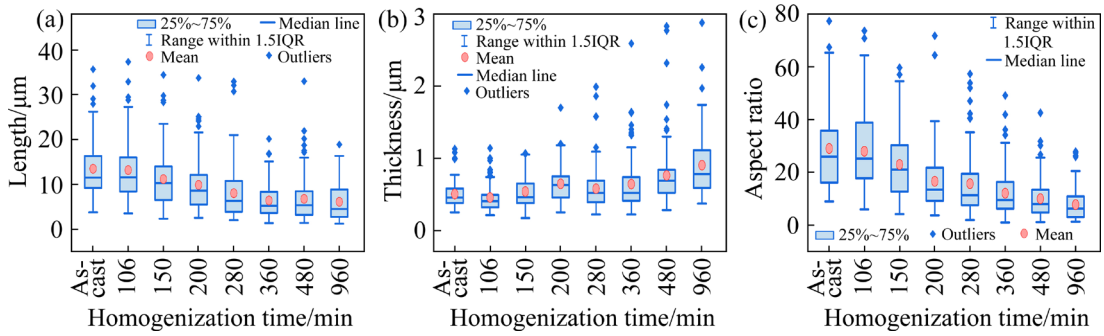

Fig. 9 Distribution of length (a), thickness (b), and aspect ratio (c) of Fe-bearing phase in alloys after homogenization at 560 °C for different time

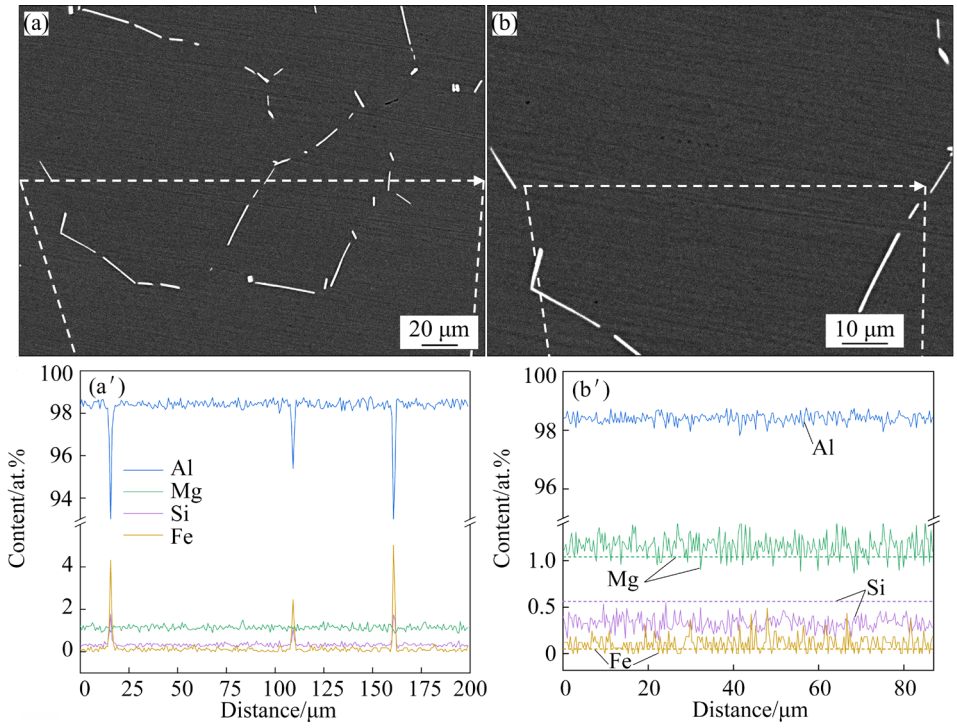

Fig. 10 Composition profiles across multiple grains (a, a′) and within grain (b, b′) in homogenized alloy after homogenization at 560 °C for 280 min

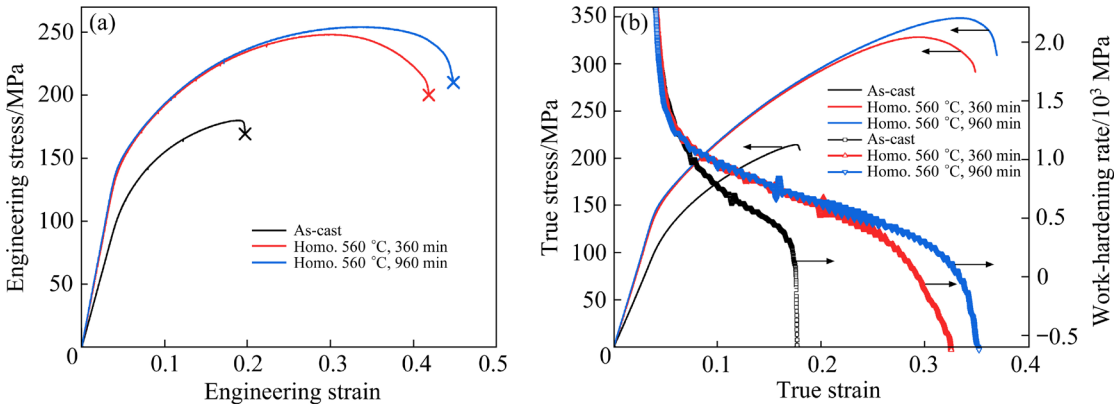

Fig. 11 Tensile properties of as-cast and homogenized alloys: (a) Engineering stress−strain curves; (b) True stress−strain and work-hardening rate curves

Table 5 Tensile test properties of as-cast and homogenized alloys

State	Yield strength/MPa	Ultimate tensile stress/MPa	Elongation/%
As-cast	112±3	178±2	12±1
Homogenized at 560 °C for 360 min	142±2	250±2	33±1
Homogenized at 560 °C for 960 min	141±1	254±1	36±1

the as-cast sample are (112±3) MPa, (178±2) MPa, and (12±1)%, respectively. After homogenization for 360 min, the YS, UTS, and El of the sample increase to (142±2) MPa, (250±2) MPa, and (33±1)%, respectively. Extending the homogenization time to 960 min, there is almost no change in YS but a slight increase in UTS and El compared to homogenization for 360 min. Figure 11(b) exhibits the true stress−strain curves and the corresponding work-hardening rate (WHR) curves. It can be seen that the as-cast sample has the lowest WHR at the same strain. It suggests that the work-hardening ability of the as-cast alloy is relatively low compared with homogenized alloys. In addition, the necking phenomenon occurs in homogenized alloys but not in as-cast alloys, implying that those two states of the alloy have different fracture mechanisms, which will be discussed later.

SEM images and EDS results of the fracture surface of the tensile test are shown in Fig. 12. It can be seen from Fig. 12(a) that some shallow equiaxial dimples are formed on the fracture surface and obvious cracks propagate along the dendrite boundaries. It is demonstrated that the fracture of the as-cast alloy occurs in an intergranular fracture manner, resulting in a relatively low elongation [23]. Moreover, the IMCs, formed during solidification, cover the fracture surface and weaken the grain boundary strength (Fig. 12(b)). Hence, the decohesion of the weak interface between IMCs and the Al matrix causes the deep cracks [23]. In addition, the brittle β-AlFeSi and Mg_2Si easily induce micro-cracks during the deformation and promote the crack propagation [16]. After homogenization, the increase in elongation is mainly attributed to the dissolution of eutectic Mg_2Si and the rounding of the Fe-bearing phase, which reduces the crack sources. Figures 12(c, d) show the dimple fracture surface in homogenized samples. The obvious dimples are formed by microvoid nucleation and coalescence [36]. The EDS results of the fracture surface (Fig. 12(e)) indicate that the dimples nucleate at the insoluble Fe-bearing phases. Moreover, deeper dimples are observed in the 960 min homogenization sample, indicating better ductility, which is consistent with the tensile results.

4 Discussion

4.1 Dendrite segregation in as-cast alloy during solidification

The ingot was obtained by the water-cooling cast. The redistribution of alloying elements and impurities occurred during the non-equilibrium solidification process, resulting in two different

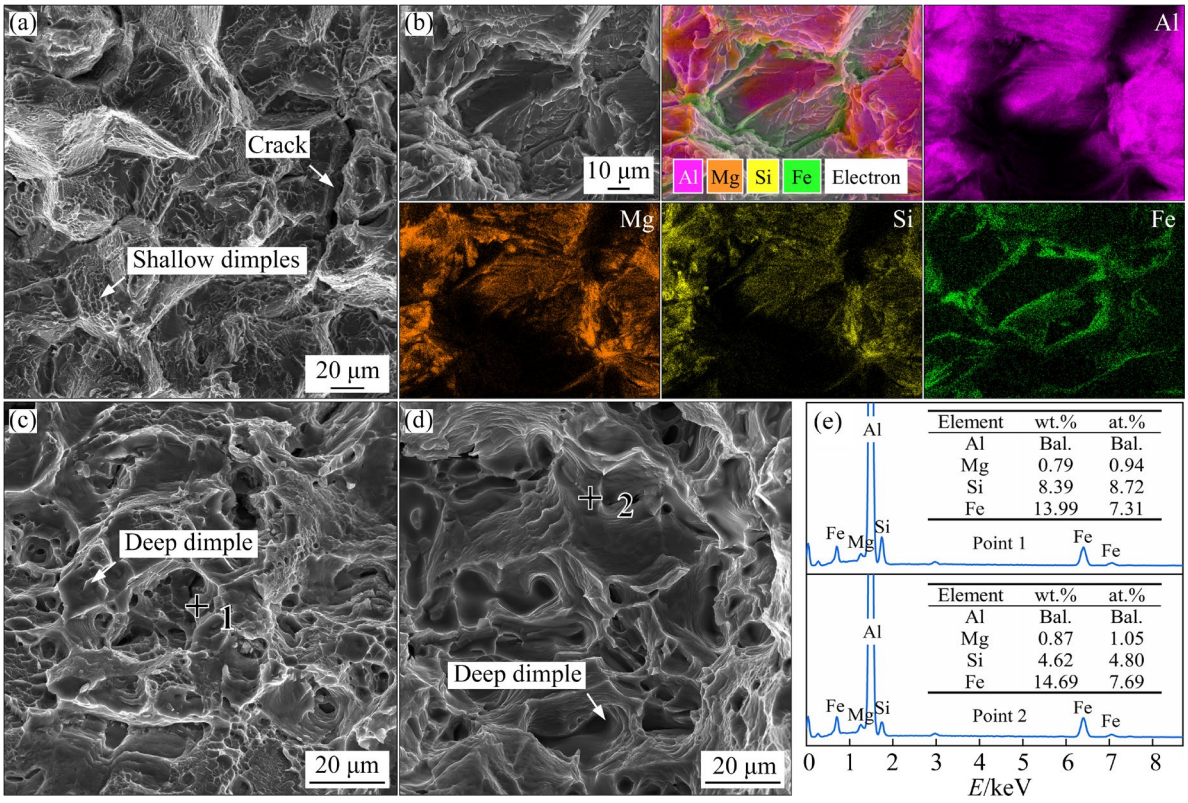

Fig. 12 Fracture surface morphologies of as-cast and homogenized alloys after tensile test: (a) As-cast alloy; (b) EDS mapping of fracture surface with IMCs adhered in as-cast alloy (Some deep regions of fracture surface cannot be characterized, resulting in missing signal) (c) 560 °C, 360 min; (d) 560 °C, 960 min; (e) EDS results

segregation phenomena. One is the inhomogeneous distribution of solute atoms (mainly Mg and Si), and the other is the formation of different IMCs (mainly eutectic Mg_2Si and β-AlFeSi) at grain boundaries (Fig. 2). Without considering the diffusion of solute in the solid phase and assuming that the liquid composition is uniform, the distribution of solute in dendrites can be described by the Scheil equation in the form as [37]

$$C_S = k_0 C_0 \left(1 - f_S\right)^{(k_0 - 1)} \quad (1)$$

where C_S is the concentration of solute in the solid phase, C_0 is the bulk concentration of alloying elements, f_S is the fraction of the solid phase, and k_0 is the equilibrium partition coefficient defined as the ratio of the concentrations of a solute in solid and liquid at equilibrium (C_S/C_L), which is used to describe the redistribution of solute during solidification. Obviously, a small k_0 (k_0<1) causes severe element segregation based on Eq. (1). k_0 for the binary Al−Mg, Al−Si, and Al−Fe system is calculated to be 0.51, 0.11, and 0.02, respectively [38], and the elemental microsegregation level from low to high is Mg, Si, and Fe. This leads to an increase in the content of Mg from the dendrite cell center towards its edge and the formation of eutectic Mg_2Si at the grain boundaries; Si mainly accumulates near the boundaries and forms eutectic Mg_2Si and β-AlFeSi at the grain boundaries; and Fe is mainly consumed by β-AlFeSi at the grain boundaries and almost has no solid solubility in the Al matrix.

4.2 Kinetics analysis of dissolution and diffusion during homogenization

Mainly eutectic Mg_2Si and β-AlFeSi are formed at grain boundaries (Fig. 1). As shown in Figs. 6 and 8, only the eutectic Mg_2Si dissolves during homogenization, while the β-AlFeSi is almost insoluble due to its high thermal stability. Accordingly, the dissolution of β-AlFeSi during homogenization is not taken into account [15,23]. The dissolution of Mg_2Si particles is modeled under the assumption that it is controlled by the diffusion of Mg in the Al matrix due to its relatively high content in Mg_2Si particles. As shown in Fig. 8(c), at

the start of the isothermal holding stage, the Mg_2Si particles are mainly distributed along the dendrite boundaries and far away from each other. Therefore, the dissolution of the phase can be considered as a diffusion process in semi-infinite space. To describe the diffusion field around the Mg_2Si particles and simplify the calculation and analysis, the morphology of Mg_2Si is regarded as sphericity, and its concentration profile at the initial stage of diffusion is displayed in Fig. 13(a). The diffusion of spherical particles can be described by the Fick's second law in a spherical coordinate system [39]. The diffusion coefficient of Mg (D) can be calculated by an Arrhenius-type equation [40]:

$$D=D_0\exp\left(-\frac{Q}{RT}\right) \tag{2}$$

where D_0=1.24 cm^2/s is the diffusion constant of Mg, Q=130.4 kJ/mol is the diffusion activation energy of the Mg, R=8.314 J/(mol·K) is the molar gas constant, and T is Kelvin temperature (K) [40].

The boundary conditions are constructed according to Fig. 13(a) as follows:

$$\begin{cases} C\left(x=r,\ 0\le t\le\infty\right)=C_{\mathrm{I}} \\ C\left(x<r,\ 0\le t\le\infty\right)=C_{\mathrm{P}} \\ C\left(x\ge r,\ t=0\right)=C_{\mathrm{M}} \end{cases} \tag{3}$$

where C is the concentration of Mg, t is the diffusion time, and r is the radius of the spherical particle. C_{I} is the Mg concentration at the particle−matrix interface, which is approximately equal to the equilibrium solubility of Mg in the matrix at the homogenization temperature and can be obtained from the solvus curve of the Al−Mg−Si diagram [12]. C_{P} is the Mg content inside the particle, and C_{M} is the initial average Mg content in the matrix, assumed to be uniform across the matrix, which can be estimated from mass conservation as [41]

$$C_{\mathrm{M}}=\frac{1}{f_{\mathrm{V}}^{\mathrm{matrix}}}\left(C_{\mathrm{A}}-f_{\mathrm{V}}^{\mathrm{Mg_2Si}}C_{\mathrm{P}}\right) \tag{4}$$

where C_{A} is the bulk concentration of Mg, $f_{\mathrm{V}}^{\mathrm{matrix}}$ and $f_{\mathrm{V}}^{\mathrm{Mg_2Si}}$ are the volume fractions of matrix and Mg_2Si particles at the start of the isothermal holding stage. This equation assumes that the sum of $f_{\mathrm{V}}^{\mathrm{matrix}}$ and $f_{\mathrm{V}}^{\mathrm{Mg_2Si}}$ equals one, namely neglecting the volume fraction of the Fe-bearing phase.

The solution of the Fick's second law can be solved according to the boundary conditions and expressed by the Gauss error function solution:

$$C_{(x,t)}=C_{\mathrm{M}}+\frac{\left(C_{\mathrm{I}}-C_{\mathrm{M}}\right)r}{x}\left(1-\mathrm{erf}\frac{x-r}{\sqrt{4Dt}}\right) \tag{5}$$

The evolution equation of the radius of the spherical phase with diffusion time is expressed as

$$\frac{r}{r_0}=1-\frac{kDt}{2r_0^2}-\frac{k}{r_0}\sqrt{\frac{Dt}{\pi}} \tag{6}$$

where k is supersaturation parameter defined as $k=2(C_{\mathrm{I}}-C_{\mathrm{M}})/(C_{\mathrm{P}}-C_{\mathrm{I}})$ [39], r_0 is the initial radius at the start of the isothermal holding stage and obtained in Fig. 8(d), which is within the range of 1 to 10 μm.

When the homogenization temperature is 560 °C, the values of C_{I}, C_{P}, and C_{M} are about 0.97, 63, and 0.27 (wt.%), respectively, and k can be calculated as about 0.02. Figure 13(b) shows the dissolution rate curves of Mg_2Si particles at the isothermal holding stage. It shows that the Mg_2Si particle with a size of 10 μm can be completely dissolved in about 10000 s during isothermal holding at 560 °C, which is close to the experimental result (~174 min).

Figure 2(b) displays the segregation of solutes (Mg and Si) in the dendrite region, and the solute concentration near the dendrite cell boundary is much higher than that inside the dendrite cell. Besides, the solute concentration gradient can be supported by the undissolved Mg_2Si particles. Therefore, the homogenization process also needs to consider eliminating the solute segregation caused by dissolved Mg_2Si particles. It is assumed that there is a solute concentration gradient inside the dendrite before the complete dissolution of Mg_2Si, which is still considered the diffusion of Mg atoms only. According to the boundary conditions derived from Fig. 13(c), the Fourier series solution of Fick's second law is as follows [42]:

$$C_{(x,t)}=C_0+\left(C_{\mathrm{I}}-C_0\right)\sin\frac{\pi x}{\lambda}\exp\left(-\frac{D\pi^2}{\lambda^2}t\right) \tag{7}$$

where C_0 is the average concentration of Mg, 2λ is the SDAS and is measured in Fig. 2. It is generally considered that the solute diffuses uniformly when the concentration difference decays to 1% of the initial state [42]. The equation describing the

diffusion process can be expressed as

$$\frac{1}{T}=\frac{R}{Q}\ln\left[\frac{\pi^2 D_0 t}{1.2(2\lambda)^2}\right] \tag{8}$$

Figure 13(d) shows the diffusion kinetic curves of Mg atoms based on Eq. (8). It suggests that the time required to eliminate the segregation of Mg atoms increases with SDAS at the given homogenization temperature. When the SDAS equals 60 μm, the Mg atoms diffuse uniformly in about 520 s at 560 °C. It is obvious that the segregation elimination time is short compared to the time for dissolving Mg_2Si particles. Accordingly, the complete dissolution time of the Mg_2Si particles is more valuable for formulating a homogenization regime.

Based on the microstructure characterization (Fig. 8), the solutes can be diffused uniformly after homogenization for about 280 min at 560 °C. In this study, the diffusion of Mg atoms is regarded as the rate-determining step (RDS) for homogenization. The kinetics analysis indicated that the acquired homogenization time is about 272 min (plus heating-up time), which agrees with the microstructure characterization results.

4.3 Evolution of Fe-bearing phase during homogenization

Figure 9 shows that the Fe-bearing phases are refined during the first 360 min of homogenization and coarsened slightly during the subsequent soaking. The variation in the geometric parameters of the Fe-bearing phase implies that its type may change. The method of determining the type of Fe-bearing phase via the Fe:Si ratio (at.%) obtained by EDS is generally accepted [10,21,22,27,43]. In this study, the EDS is used to distinguish the type of Fe-bearing phase and determine the degree of transformation of β to α. The Fe:Si ratios of Fe-bearing phases are plotted in Fig. 14(a). The Fe:Si ratios of the Fe-bearing phases increase after being homogenized at 560 °C for 960 min. However, the Fe:Si ratios of most Fe-bearing phases are lower than those of α-AlFeSi. It suggests that only a small portion of β-AlFeSi particles formed during solidification is converted to α-AlFeSi particles. The XRD result for the homogenized alloy also indicates that β-AlFeSi is still the dominant Fe-bearing phase in the alloy (Fig. 14(b)). Accordingly, the majority of the β-AlFeSi phases merely undergo morphological alterations. Due to the difference in solute concentration at the

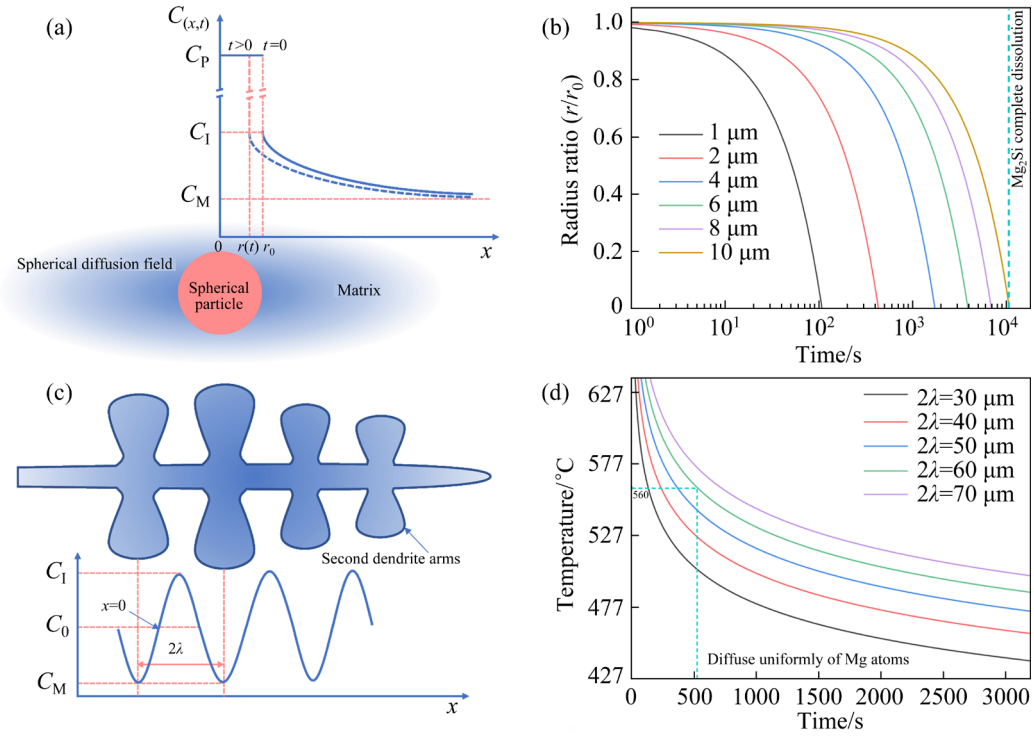

Fig. 13 (a) Schematic diagram of solute concentration in vicinity of spherical particles; (b) Dissolution rate curve of Mg_2Si particles at 560 °C; (c) Schematic diagram of solute concentration between second dendrite arms; (d) Diffusion kinetics curves of Mg atoms

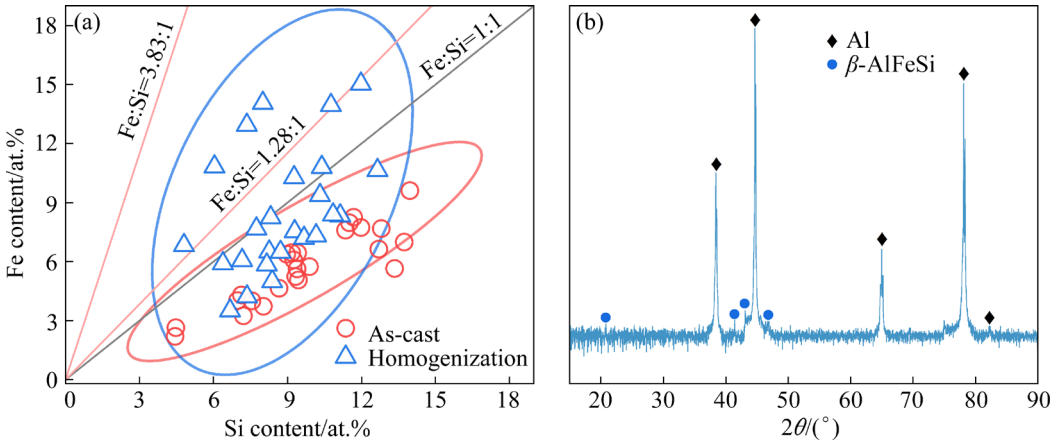

Fig. 14 (a) Fe and Si contents in Fe-bearing phases of as-cast and homogenized (at 560 °C for 960 min) samples (The Fe:Si atomic ratios of α- and β-AlFeSi are plotted in red and black lines, respectively); (b) XRD pattern of homogenized alloy

β-AlFeSi/Al interface, solute atoms are diffused from β-AlFeSi into the Al matrix, which causes β-AlFeSi to dissolve and transform [8]. Since the diffusion coefficient of Fe is lower than that of Si [8], the Si in the Fe-bearing phase diffuses into the Al matrix faster, and thus it is likely that the diffusion of Fe is the RDS of the dissolution process of β-AlFeSi. It is noteworthy that longer soaking time leads to the coarsening of Fe-bearing phases. On the contrary, it also results in a more rounded morphology of the Fe-bearing phases, which hardly affects the tensile properties of the alloy (Table 5). Considering the evolution of microstructure and the resource savings, the more suitable homogenization parameters are determined as 560 °C for 360 min for the studied alloy.

4.4 Tensile behavior of as-cast and homogenized alloys

As discussed above, the dilute Al−Mg−Si alloy undergoes three microstructural changes when subjected to homogenization, including precipitation and dissolution of the particles during the heating-up stage, dissolution of eutectic Mg_2Si and solutes uniform, as well as the transformation of β-AlFeSi during the isothermal holding stage. The tensile data and fracture observations indicate that the mechanical properties of the studied alloys are mainly affected by the extent of the dissolution of eutectic Mg_2Si and the rounding of the Fe-bearing phase. Besides, the samples were quenched in water after the isothermal holding and then stored at room temperature for a period of time before the tensile tests, resulting in cluster-hardening of the samples [44]. The microstructure evolution causes the homogenized alloys to exhibit different flow stresses and work-hardening behaviors than as-cast alloys. As shown in Fig. 11(b), the WHR curves of both as-cast and homogenized alloys show a rapid decrease in the elastic-plastic transition range and then exhibit an approximately linear decrease in the plastic range. The mechanism of the rapid decrease mainly corresponds to the cross-slip of dislocations, while the linear decrease mainly corresponds to dynamic recovery, which is induced by dislocation annihilation and the cross-slip of dislocations bypassing the barriers to relax the inner stress field [45]. It is clear that homogenized alloys have a relatively low linear decrease rate in their WHR curves compared to as-cast alloys. That is because the solid solute atoms and clusters in homogenized alloys make the annihilation process more difficult, thereby reducing the dynamic recovery rate [46]. It is worth noting that although the ductility of the homogenized samples has been greatly improved, the solid-solution strengthening and cluster-hardening result in an increase in deformation resistance.

5 Conclusions

(1) Mg_2Si and β-AlFeSi are the main intermetallic compounds in as-cast alloys, which are mainly distributed at grain boundaries. Inside the dendrite cell, the concentration of Mg gradually

increases from the center of the dendrite cell to its edge, Si mainly segregates near the dendrite cell boundary, and the content of Fe remains constant and close to zero. Only the segregation of Mg can be fully eliminated after homogenization treatment, while Fe and part of Si still exist in the form of insoluble Fe-bearing phases.

(2) The studied alloy homogenized at 560 °C for 280 min is sufficient to dissolve eutectic Mg_2Si fully without overburning. For the isothermal holding stage at 560 °C, the prediction results derived from kinetic equations demonstrated that the Mg_2Si particles can be dissolved completely in about 10000 s (~166.7 min) and the Mg atoms diffuse uniformly in about 520 s (~8.7 min). The sum of the two parts is consistent with the experiment results (174 min).

(3) The β-AlFeSi in the studied alloy exhibits high thermal stability and mainly undergoes dissolution and coarsening during homogenization at 560 °C. Only a small amount of β-AlFeSi is converted to α-AlFeSi after homogenization for 960 min. The optimal homogenization parameters for the studied alloy are 560 °C and 360 min, when considering the evolution of the microstructure and the resource savings.

(4) The dissolution of Mg_2Si and the rounding of Fe-bearing phases during homogenization cause a significant increase in the ductility of the studied alloy. The increase in strength is caused by cluster hardening after room temperature storage.

CRediT authorship contribution statement

Dong JIN: Conceptualization, Methodology, Data curation, Writing − Original draft preparation, Formal analysis, Investigation, Writing − Reviewing and editing. **Hong-ying LI:** Supervision, Project administration, Funding acquisition, Resources, Methodology, Writing − Reviewing and editing; **Zhi-xiang ZHU:** Supervision, Project administration, Funding acquisition; **Chang-long YANG:** Supervision, Project administration, Funding acquisition; **Yao-jun MIAO:** Supervision, Project administration; **Chao XU:** Project administration, Funding acquisition; **Bao-an CHEN:** Supervision, Project administration; **Zhen LIU:** Project administration.

Declaration of competing interest

The authors declare that they have no known competing financial interests or personal relationships that could have appeared to influence the work reported in this paper.

Acknowledgments

This work was financially supported by State Grid Corporation of China (No. 5500-202128250A-0-0-00).

References

[1] KARABAY S. Modification of AA-6201 alloy for manufacturing of high conductivity and extra high conductivity wires with property of high tensile stress after artificial aging heat treatment for all-aluminium alloy conductors [J]. Materials & Design, 2006, 27(10): 821−832.

[2] KARABAY S. Influence of AlB_2 compound on elimination of incoherent precipitation in artificial aging of wires drawn from redraw rod extruded from billets cast of alloy AA-6101 by vertical direct chill casting [J]. Materials & Design, 2008, 29(7): 1364−1375.

[3] SAUVAGE X, BOBRUK E V, MURASHKIN M Y, NASEDKINA Y, ENIKEEV N A, VALIEV R Z. Optimization of electrical conductivity and strength combination by structure design at the nanoscale in Al−Mg−Si alloys [J]. Acta Materialia, 2015, 98: 355−366.

[4] KHANGHOLI S N, JAVIDANI M, MALTAIS A, CHEN X G. Effects of natural aging and pre-aging on the strength and electrical conductivity in Al−Mg−Si AA6201 conductor alloys [J]. Materials Science and Engineering A, 2021, 820: 141538.

[5] LIU C L, AZIZI-ALIZAMINI H, PARSON N C, POOLE W J, DU Q. Microstructure evolution during homogenization of Al−Mg−Si−Mn−Fe alloys: Modelling and experimental results [J]. Transactions of Nonferrous Metals Society of China, 2017, 27(4): 747−753.

[6] GRANDFIELD J F, ESKIN D G, BAINBRIDGE I F. Direct-chill casting of light alloys: Science and technology [M]. Hoboken, New Jersey: John Wiley and Sons, Inc., 2013.

[7] HAIDEMENOPOULOS G N, KAMOUTSI H, ZERVAKI A D. Simulation of the transformation of iron intermetallics during homogenization of 6xxx series extrudable aluminum alloys [J]. Journal of Materials Processing Technology, 2012, 212(11): 2255−2260.

[8] BAYAT N, CARLBERG T, CIESLAR M. In-situ study of phase transformations during homogenization of 6005 and 6082 Al alloys [J]. Journal of Alloys and Compounds, 2017, 725: 504−509.

[9] DONS A L. The Alstruc homogenization model for industrial aluminum alloys [J]. Journal of Light Metals, 2001, 1(2): 133−149.

[10] BIROL Y. The effect of homogenization practice on the microstructure of AA6063 billets [J]. Journal of Materials Processing Technology, 2004, 148(2): 250−258.

[11] MOHAMED A M A, SAMUEL F H, AL-KAHTANI S. Influence of Mg and solution heat treatment on the occurrence of incipient melting in Al−Si−Cu−Mg cast alloys [J]. Materials Science and Engineering A, 2012, 543: 22−34.

[12] BELOV N A, ESKIN D G, AKSENOV A A.

Multicomponent phase diagrams: Applications for commercial aluminum alloys [M]. Amsterdam: Elsevier, 2005.

[13] ZHU H L, COUPER M J, DAHLE A K. Effect of process variables on Mg−Si particles and extrudability of 6xxx series aluminum extrusions [J]. JOM, 2011, 63 (11): 66−71.

[14] AMADO M N, DAROQUI F. Revision of the solvus limit of Al−Mg_2Si pseudo binary phase diagram [J]. Procedia Materials Science, 2015, 8: 1079−1088.

[15] QIN Jian, NAGAUMI H, YU Cheng-bin, LIU Fang-zhen, LI Yi-feng, WANG Lin-sheng. Coarsening behavior of Mg_2Si precipitates during post homogenization cooling process in Al−Mg−Si alloy [J]. Journal of Alloys and Compounds, 2022, 902: 162851.

[16] ÖSTERREICHER J A, KUMAR M, SCHIFFL A, SCHWARZ S, BOURRET G R. Secondary precipitation during homogenization of Al−Mg−Si alloys: Influence on high temperature flow stress [J]. Materials Science and Engineering A, 2017, 687: 175−180.

[17] HE Yang, JIA Zhi-hong, SANDERS R E, LIU Ying-ying, DING Li-peng, XING Yuan, LIU Qing. Quantitative study of dissolution of Mg_2Si during solution treatment in AA6014 alloy [J]. Journal of Alloys and Compounds, 2017, 703: 272−279.

[18] ROMETSCH P A, ARNBERG L, ZHANG D L. Modelling dissolution of Mg_2Si and homogenization in Al−Si−Mg casting alloys [J]. International Journal of Cast Metals Research, 1999, 12(1): 1−8.

[19] SAMARAS S N, HAIDEMENOPOULOS G N. Modelling of microsegregation and homogenization of 6061 extrudable Al-alloy [J]. Journal of Materials Processing Technology, 2007, 194(1/2/3): 63−73.

[20] ZHANG Xu-kai, GUO Ming-xing, ZHANG Ji-shan, ZHUANG Lin-zhong. Dissolution of precipitates during solution treatment of Al−Mg−Si−Cu alloys [J]. Metallurgical and Materials Transactions B, 2016, 47: 608−620.

[21] KUIJPERS N C W, VERMOLEN F J, VUIK K, VAN DER ZWAAG S. A model of the β-AlFeSi to α-Al(FeMn) Si transformation in Al−Mg−Si alloys [J]. Materials Transactions, 2003, 44(7): 1448−1456.

[22] KUIJPERS N C W, VERMOLEN F J, VUIK C, KOENIS P T G, NILSEN K E, VAN DER ZWAAG S. The dependence of the β-AlFeSi to α-Al(FeMn)Si transformation kinetics in Al−Mg−Si alloys on the alloying elements [J]. Materials Science and Engineering A, 2005, 394(1/2): 9−19.

[23] RADETIĆ T, POPOVIĆ M, ALIL A, MARKOLI B, NAGLIČ I, ROMHANJI E. Effect of homogenization temperature on microstructure and mechanical properties of Al−Mg−Si alloy containing low-melting point elements [J]. Journal of Alloys and Compounds, 2022, 902: 163719.

[24] HOSSEINIFAR M, MALAKHOV D V. The sequence of intermetallics formation during the solidification of an Al−Mg−Si alloy containing La [J]. Metallurgical and Materials Transactions A, 2011, 42: 825−833.

[25] KRÁLÍK R, KŘIVSKÁ B, BAJTOŠOVÁ L, ŠLAPÁKOVÁ M, CIESLAR M. Homogenization of twin-roll cast AA8079 aluminum alloy studied by in-situ TEM [J]. Transactions of Nonferrous Metals Society of China, 2022, 32(7): 2138−2149.

[26] VERMA A, KUMAR S, GRANT P S, O'REILLY K A Q. Influence of cooling rate on the Fe intermetallic formation in an AA6063 Al alloy [J]. Journal of Alloys and Compounds, 2013, 555: 274−282.

[27] LIU Ze-tian, WANG Cheng, LUO Qun, YOU Jiang, ZHOU Xiao-li, XU Jin, MO Yuan-ting, SONG Jia-Wang, ZHA Min, WANG Hui-yuan. Effects of Mg contents on the microstructure evolution and Fe–bearing phase selection of Al−Mg−Si−Fe alloys under sub–rapid solidification [J]. Materialia, 2020, 13: 100850.

[28] MENG Yi, CUI Jian-zhong, ZHAO Zhi-hao. Effect of Fe on microstructures and mechanical properties of an Al−Mg−Si−Cu−Cr−Zr alloy prepared by low frequency electromagnetic casting [J]. Journal of Materials Research, 2017, 32(11): 2067−2078.

[29] ZHU Liang, Guo Ming-xing, ZHANG Ji-shan. The multi-scale Si-containing phases-assisted improvement in the microstructure and mechanical properties of Al−Mg−xSi−Cu−Zn alloys [J]. Materials Science and Engineering A, 2021, 826: 142013.

[30] GRIGER Á, STEFÁNIAY V. Equilibrium and non-equilibrium intermetallic phases in Al−Fe and Al−Fe−Si alloys [J]. Journal of Materials Science, 1996, 31: 6645−6652.

[31] ZAJAC S, HUTCHINSON B, JOHANSSON A, GULLMAN L O. Microstructure control and extrudability of Al−Mg−Si alloys microalloyed with manganese [J]. Materials Science and Technology, 1994, 10(4): 323−333.

[32] GAO L, HARADA Y, KUMAI S. Microstructural characterization of aluminum alloys using Weck's reagent. Part I: Applications [J]. Materials Characterization, 2015, 107: 426−433.

[33] ALLEN C M, O'REILLY K A Q, CANTOR B, EVANS P V. Intermetallic phase selection in 1xxx Al alloys [J]. Progress in Materials Science, 1998, 43(2): 89−170.

[34] PEREZ M. Gibbs−Thomson effects in phase transformations [J]. Scripta Materialia, 2005, 52(8): 709−712.

[35] UTTARASAK K, CHONGCHITNAN W, MATSUDA K, CHAIRUANGSRI T, KAJORNCHAIYAKUL J, BANJONGPRASERT C. Evolution of Fe-containing intermetallic phases and abnormal grain growth in 6063 aluminum alloy during homogenization [J]. Results in Physics, 2019, 15: 102535.

[36] LIU Yu-xuan, WANG Ri-chu, PENG Chao-qun, CAI Zhi-yong, ZHOU Zhao-hui, LI Xiao-geng, CAO Xuan-yang. Microstructures and mechanical properties of in-situ TiB_2/Al−xSi−0.3Mg composites [J]. Transactions of Nonferrous Metals Society of China, 2021, 31(2): 331−344.

[37] ZHOU Yi-ran, TIAN Ni, LIU Wei, ZENG Yu, WANG Guang-dong, HAN Shi-da, ZHAO Gang, QIN Gao-wu. Mechanism of heterogeneous distribution of Cr-containing dispersoids in DC casting 7475 aluminum alloy [J]. Transactions of Nonferrous Metals Society of China, 2022, 32(5): 1416−1427.

[38] EASTON M, STJOHN D. Grain refinement of aluminum alloys: Part I. the nucleant and solute paradigms—A review of the literature [J]. Metallurgical and Materials Transactions A, 1999, 30: 1613−1623.

[39] WHELAN M J. On the kinetics of precipitate dissolution [J].

Metal Science Journal, 1969, 3: 95−97.
[40] GALE W F, TOTEMEIER T C. Smithells metals reference book [M]. London: Elsevier Butterworth-Heinemann, 2004.
[41] R. GHIAASIAAN, SHANKAR S. Structure-property models in Al−Zn−Mg−Cu alloys: A critical experimental assessment of shape castings [J]. Materials Science and Engineering A, 2018, 733: 235−245.
[42] FU Rong, HUANG Yuan-chun, LIU Yu, LI Hui, WANG Zhi-wen. Influence of homogenization treatment on microstructure and recrystallization behavior of 2195 Al−Li alloy [J]. Transactions of Nonferrous Metals Society of China, 2023, 33(8): 2255−2271.
[43] LI Quan, WANG Jun-sheng, LIU Xin-xiu, WANG Bing. Minimizing detrimental impacts of β-Fe in Al−Mg−Si alloy by combining thermal and compression processes [J]. Materials Characterization, 2023, 198: 112752.
[44] STARINK M J, CAO L F, ROMETSCH P A. A model for the thermodynamics of and strengthening due to co-clusters in Al−Mg−Si-based alloys [J]. Acta Materialia, 2012, 60(10): 4194−4207.
[45] BAHRAMI A, MIROUX A, SIETSMA J. Modeling of strain hardening in the aluminum alloy AA6061 [J]. Metallurgical and Materials Transactions A, 2013, 44: 2409−2417.
[46] ZHU Liang, GUO Ming-xing, WU Yuan, ZHU Hui-hui, ZHANG Ji-shan. Synergy of homogeneous/heterogeneous nucleation in Al−Mg−xSi−Cu−Zn alloys with rapid age-hardening response [J]. Materials Characterization, 2022, 192: 112224.

不同均匀化参数下平衡 Al−Mg−Si 合金的组织演变和拉伸行为

靳 东[1]，李红英[1]，祝志祥[2]，杨长龙[3]，缪姚军[4]，许 超[3]，陈保安[2]，刘 臻[5]

1. 中南大学 材料科学与工程学院，长沙 410083；
2. 国网智能电网研究院有限公司 先进输电技术国家重点实验室，北京 102209；
3. 国网辽宁省电力有限公司，沈阳 110042；
4. 江苏中天科技股份有限公司，南通 226010；
5. 中国电力科学研究院有限公司，北京 100192

摘 要：采用金相显微镜、扫描电镜、X 射线衍射、电子探针、差示扫描量热仪、电导率测试和拉伸测试，研究均匀化参数对平衡 Al−Mg−Si 合金组织演变和拉伸行为的影响。结果表明，Mg_2Si 和 β-AlFeSi 是铸态组织中的主要金属间化合物，枝晶内主要存在 Mg 的溶质偏析。动力学模型对 Mg_2Si 颗粒完全溶解时间的预测与实验结果一致。合金中的 β-AlFeSi 具有高的热稳定性，在 560 ℃进行均匀化时主要发生溶解和粗化，仅少量转变为 α-AlFeSi。综合考虑到组织演变和资源节约，确定最优均匀化制度为 560 ℃和 360 min。均匀化后合金的强度和塑性均有所提高。

关键词：Al−Mg−Si 合金；均匀化；动力学模型；富铁相；拉伸行为

(Edited by Xiang-qun LI)